# Precipitation and Latent Heating Distributions from Satellite Passive Microwave Radiometry. Part II: Evaluation of Estimates Using Independent Data

SONG YANG

*School of Computational Science, George Mason University, Fairfax, Virginia*

WILLIAM S. OLSON

*Joint Center for Earth Systems Technology, University of Maryland, Baltimore County, Baltimore, Maryland*

JIAN-JIAN WANG

*Goddard Earth Sciences and Technology Center, University of Maryland, Baltimore County, Baltimore, Maryland*

THOMAS L. BELL AND ERIC A. SMITH

*Goddard Space Flight Center, Greenbelt, Maryland*

CHRISTIAN D. KUMMEROW

*Colorado State University, Fort Collins, Colorado*

(Manuscript received 11 February 2005, in final form 2 September 2005)

ABSTRACT

Rainfall rate estimates from spaceborne microwave radiometers are generally accepted as reliable by a majority of the atmospheric science community. One of the Tropical Rainfall Measuring Mission (TRMM) facility rain-rate algorithms is based upon passive microwave observations from the TRMM Microwave Imager (TMI). In Part I of this series, improvements of the TMI algorithm that are required to introduce latent heating as an additional algorithm product are described. Here, estimates of surface rain rate, convective proportion, and latent heating are evaluated using independent ground-based estimates and satellite products. Instantaneous, 0.5°-resolution estimates of surface rain rate over ocean from the improved TMI algorithm are well correlated with independent radar estimates ($r \sim 0.88$ over the Tropics), but bias reduction is the most significant improvement over earlier algorithms. The bias reduction is attributed to the greater breadth of cloud-resolving model simulations that support the improved algorithm and the more consistent and specific convective/stratiform rain separation method utilized. The bias of monthly 2.5°-resolution estimates is similarly reduced, with comparable correlations to radar estimates. Although the amount of independent latent heating data is limited, TMI-estimated latent heating profiles compare favorably with instantaneous estimates based upon dual-Doppler radar observations, and time series of surface rain-rate and heating profiles are generally consistent with those derived from rawinsonde analyses. Still, some biases in profile shape are evident, and these may be resolved with (a) additional contextual information brought to the estimation problem and/or (b) physically consistent and representative databases supporting the algorithm. A model of the random error in instantaneous 0.5°-resolution rain-rate estimates appears to be consistent with the levels of error determined from TMI comparisons with collocated radar. Error model modifications for nonraining situations will be required, however. Sampling error represents only a portion of the total error in monthly 2.5°-resolution TMI estimates; the remaining error is attributed to random and systematic algorithm errors arising from the physical inconsistency and/or nonrepresentativeness of cloud-resolving-model-simulated profiles that support the algorithm.

*Corresponding author address:* Dr. Song Yang, Goddard Space Flight Center, Code 613.1, Greenbelt, MD 20771.
E-mail: ysong@agnes.gsfc.nasa.gov

## 1. Introduction

In Olson et al. (2006, hereinafter Part I), an improved method for inferring precipitation and atmospheric latent heating profiles from satellite passive microwave radiometer measurements was described, and random errors resulting from algorithm and sampling deficiencies were estimated. This method represents the current [version 6 (or V6)] Tropical Rainfall Measuring Mission (TRMM) facility algorithm applied to passive microwave observations from the TRMM Microwave Imager (TMI) over oceanic regions. The preceding TMI algorithm [version 5 (V5)] produced estimates of surface rain rates and vertical precipitation profiles but not latent heating profiles. In addition to TMI algorithm improvements, Part I also describes components of a model to describe the random errors in (a) instantaneous half-degree algorithm estimates suitable for data assimilation applications, and (b) monthly 2.5°-resolution algorithm estimates, designed for climate analyses. The error estimates in Part I are largely theoretical, based upon the algorithm's Bayesian formulation and applications of the algorithm to synthetic data.

In addition to the TMI, the TRMM observatory includes the first spaceborne weather radar, or precipitation radar (PR). Because the PR provides much higher resolution depictions of both vertical and horizontal precipitation structures than the TMI, rain-rate estimates based upon PR observations should in principle provide more accurate estimates of precipitation. However, contamination of the PR observations by surface backscatter at off-nadir viewing angles restricts the PR's useful swath width to approximately 215 km for a nominal TRMM satellite altitude of 350 km. By contrast, the TMI and most current satellite microwave imagers are conically scanning, which allows for uniform-resolution observations over swaths $\sim 10^3$ km wide for nominal satellite altitudes. Because of their limited swath width and additional weight and power consumption, spaceborne radars assume the role of "calibrators" of passive microwave precipitation estimates, while the passive radiometers, already a component of several polar-orbiting observatories, provide more extensive sampling of precipitation events over the globe.

Although the PR provides an extensive set of comparative data, passive microwave estimates of precipitation and latent heating can also be evaluated using independent estimates derived from ground-based radars (including single- and dual-Doppler configurations) and rawinsonde observation networks. As part of TRMM, radar data are collected continuously at four ground validation sites in the Tropics. These data have been supplemented by dual-Doppler radar and rawinsonde observations from field campaigns in the South China Sea (SCS), western Brazil, and the vicinity of the Kwajalein Atoll.

Here, in the second part of this series, V6 and V5 TMI-estimated rain rates and latent heating profiles are compared with coincident estimates from both ground-based systems and PR-based algorithms as a test of consistency. It is not possible to "validate" the TMI estimates in a strict sense, because validation requires comparison with independent measurements that have much less uncertainty than the TMI estimates, and this is not always the case. On the other hand, the independent measurements do provide a useful reference to help identify possible biases and the general levels of uncertainty associated with the TMI estimates, and algorithm random errors derived from the independent measurements can be related to the theoretical error estimates of Part I. Also, the independent data are used to illustrate the changes in rain-rate estimates derived from the current V6 TMI method relative to the previous technique from which it is descended (V5). The two parts of this series, taken together, provide a more complete picture of the strengths and limitations of the TMI algorithm and how errors in precipitation/latent heating estimates can be quantified for applications such as data assimilation and climate analysis.

In section 2, the various data sources and products utilized in this study are described in detail. TMI surface rain-rate estimates are compared with surface radar and PR estimates at different time and space resolutions in section 3. Section 4 is devoted to comparisons of V6 TMI rain-rate and latent heating profile estimates with independent estimates from ground-based systems, and a summary and discussion are provided in section 5.

## 2. Datasets

The focus of the current study is on the estimation of three parameters from satellite data: the surface rainfall rate, the convective proportion of rain, and the vertical profile of latent heating, defined here as the apparent heat source less the radiative heating rate, or $Q_1 - Q_R$; see Yanai et al. (1973). The quantity $Q_1 - Q_R$ thus emphasizes the heating resulting from phase changes of the water substance in precipitating clouds. The surface rainfall rate and the convective proportion of rain are standard outputs of both the V5 and V6 TMI algorithms. The V5 TMI algorithm is described in Kummerow et al. (2001), and the modifications that resulted in V6 are described in Part I. Because of key improvements in the classification of convective/stratiform rain

regions and total rain area within the TMI footprint, a profile of latent heating is derived as one of the standard products of V6 over ocean, while no such standard latent heating product was created based upon V5.

The sampling resolution of the TMI is about 14 km along track and 4.5 km cross track, and the spatial resolution of each measurement varies with channel frequency from about 48 km at 10.7 GHz to 6 km at 85.5 GHz. The V6 TMI precipitation products are designed to have an intermediate spatial resolution of 14 km × 14 km (see Part I), while V5 products have comparable resolution.

### *a. Surface rainfall*

To demonstrate the performance of the TMI algorithm, precipitation products from V5 and V6 are compared with independent rain estimates at different time and space scales. The traditional "ground truth" for surface rain rates is derived from ground validation (GV) radar, a key element in the algorithm evaluation process. There are four GV field sites serviced by the TRMM validation project; however, the Kwajalein Atoll site was specifically designed to provide data characteristic of a tropical oceanic environment. A map of the Kwajalein field site is shown in Fig. 1. Standard version-3 TRMM GV output products are derived from each radar volume out to a range of 150 km; surface rain-rate and convective/stratiform classification are interpolated to a 2 km × 2 km resolution horizontal grid. The radar-sampling interval is 10 min, and so the radar map closest to the TRMM satellite overpass time is utilized for intercomparisons. In the current study, all significant rain events observed coincidentally by the TMI and the Kwajalein radar during 1998 are collected, yielding 21 events. The Kwajalein GV radar rain rates are adjusted using coincident rain gauge measurements to remove the radar–rain gauge bias over monthly periods; see Wolff et al. (2005). Because of the limited number of functioning rain gauges in particular months, however, the bulk adjustment of GV radar reflectivity–rain rate relations (convective and stratiform) was based upon coincident radar and rain gauge data from multiple months. Over 1998 as a whole, the (unadjusted) radar-to-rain gauge ratio based upon all coincident radar–rain gauge pairs was 1.24 with a correlation of 0.98.

Because the TRMM GV sites yield rain-rate and convective proportion information at only a limited number of locations in the Tropics, products derived from the spaceborne PR are also considered in the current investigation. Surface rain rate at each PR footprint location is a standard TRMM product derived using the

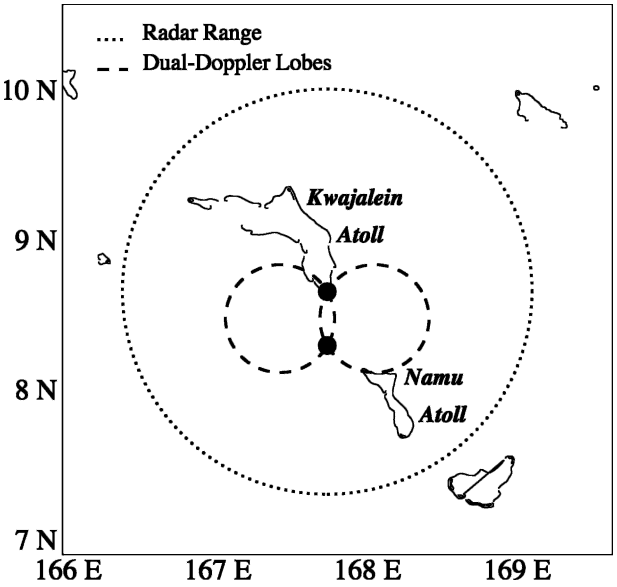


FIG. 1. Map of the Kwajalein Atoll and vicinity, showing the locations of radars on Kwajalein and the Research Vessel *Ron H. Brown* during cruise 1, the domain of rain observations provided by the Kwajalein radar, and the dual-Doppler coverage provided by the two radars. This was the configuration of radars during the period of cruise 1 in the KWAJEX field campaign.

algorithm of Iguchi et al. (2000). The classification of each PR footprint as convective/stratiform/undetermined is also a standard product, based upon the method of Awaka et al. (1998). The PR V5 rain rates and convective/stratiform classifications are used exclusively for intercomparisons, because more recent versions were not available during the course of the study. The scan geometry and sampling rate of the PR lead to footprints spaced approximately 4.3 km cross and down track, over a 215-km-wide swath centered within the 760-km-wide TMI swath; therefore, TMI and PR observations over the PR swath are nearly coincident in time and space, aside from the ~1 min offset in observation time caused by the difference in the scan geometries of the sensors. The PR measurements themselves have an intrinsic spatial resolution of about 4.3 km, because of the diffraction limitation of the instrument. In a comparison of PR near-surface rain rates and collocated Weather Surveillance Radar-1988 Doppler (WSR-88D) radar at Melbourne, Florida (one of the TRMM ground validation radars), Liao et al. (2001) noted a high bias of 3% and a standard error of 44% in PR rain estimates on an overpass-by-overpass basis, with a correlation between the PR and ground validation rain estimates of 0.95. The relatively large standard error percentage results from the large population of light rains that contribute to the mean rain rate, and so this statistic does not necessarily reflect the good con-

sistency between PR and ground radar at higher rain rates. Schumacher and Houze (2000) also noted good agreement between PR and ground validation radar estimates of rain rates at Kwajalein. They reported biases of 6% or less, depending on the reflectivity–rain rate relations applied to the radar data, and a PR–ground validation radar rain-rate correlation of 0.96. In both the Melbourne and Kwajalein radar comparisons, the mean convective and stratiform rain rates from PR agreed with the ground radar amounts to within 21%.

Following the discussion of estimated TMI product uncertainties in Part I, intercomparisons of TMI precipitation products and independent estimates are carried out at time and space resolutions that reflect potential applications of the products. Assimilation of surface rain-rate or latent heating profiles into global climate or numerical weather prediction model analyses/forecasts requires instantaneous products at half-degree (or comparable) spatial resolution (see Krishnamurti et al. 2001; Hou et al. 2004). Consequently, instantaneous rainfall rates and convective proportion estimates at 0.5° resolution are compared in this study. Because the spatial sampling of TMI, GV radar, and PR are all relatively fine over 0.5° latitude × 0.5° longitude grid boxes, instantaneous precipitation estimates from each of the three sensors are simply averaged to obtain half-degree products for the intercomparisons.

Alternatively, climate or large-scale analysis studies may only require lower-resolution estimates. When TMI precipitation estimates are averaged over the period of 1 month in 2.5° latitude × 2.5° longitude grid boxes, the random error resulting from the limited information content of the radiometer data becomes fairly negligible, although sampling error can be significant; see Part I. Therefore, as a test of a proxy climate product, monthly mean 2.5° TMI estimates are compared with independent estimates from the PR. These products are created by averaging all instantaneous precipitation estimates falling in a particular 2.5° latitude × 2.5° longitude box in a specified month.

At either instantaneous 0.5°- or monthly 2.5°-resolution, precipitation products are not included in statistics if both the TMI and the independent product are nonraining pairs. Because, at most locations over the tropical and subtropical oceans, rain occurs less than 15% of the time [Petty (1995)], eliminating nonraining pairs in the statistics emphasizes the algorithm's ability to quantify precipitation where it is raining. When instantaneous imagery is compared, either GV radar or PR estimates are averaged within a 196 km$^2$ (14 km × 14 km) circular area centered on a given TMI observation to approximate the resolution of the TMI instantaneous, footprint-scale estimates.

### b. Latent heating

The evaluation of latent heating estimates from satellite observations is always a difficult challenge, since there exist no independent and direct estimates of latent heating. Yang and Smith (1999b) approached this problem by analyzing the evolution of 3D latent heating structures for well-known climate systems to determine qualitatively the reliability of their latent heating estimates. Two alternative approaches are used to evaluate TMI latent heating rate estimates in this study. The first method is founded on the assumption that the dominant contribution to diabatic heating comes from the vertical advection of dry static energy (e.g., Cifelli and Rutledge 1998). In this approximation,

$$w\frac{\partial s}{\partial z} \approx c_p Q_1, \tag{1}$$

where $w$ is the vertical velocity, $s$ is the dry static energy ($c_pT + gz$), and $z$ is altitude. Here, $c_p$ is the specific heat of air at constant pressure, $T$ is temperature, and $g$ is the acceleration of gravity. Note that additional terms on the left-hand side of (1), including the storage and horizontal advection of dry static energy, can lead to errors in heating estimates. Although these additional terms are relatively small throughout most of the troposphere, they may account for as much as 20% of the peak heating based on the analysis of tropical anvils by Johnson and Young (1983). The vertical velocity in (1) can be calculated using dual-Doppler radar observations. Dual-Doppler analysis yields the horizontal wind speed and direction; by vertically integrating the divergence of the horizontal wind, one obtains the vertical velocity subject to a prescribed vertical velocity at the top or bottom of the air column (Doviak et al. 1976; Davies-Jones 1979). The dry static energy is calculated from sounding data coinciding with the dual-Doppler observations. Combining the dual-Doppler vertical velocities and dry static energy gradient in (1) yields a "dual-Doppler study" ("DDS") estimate of latent heating.

During the TRMM field campaign at Kwajalein (KWAJEX; 23 July–15 September 1999), an S-band radar on the Kwajalein Atoll and a C-band radar aboard the Research Vessel (R/V) *Ron H. Brown* provided dual-Doppler coverage of precipitation systems over the Pacific Ocean. During cruise 1 (28 July–19 August, 1999) of KWAJEX, the R/V *Ron H. Brown* was positioned 40 km south of the Kwajalein radar site, and this configuration allowed for dual-Doppler coverage within the two 80-km-diameter circular "lobes" for which the crossing angle of radar rays was greater than 30° (see Fig. 1). Unfortunately, there were relatively

few dual-Doppler radar observations of KWAJEX rain events that coincided with TRMM satellite overpasses. From KWAJEX, only five such events have been identified, and only two involve organized mesoscale convective systems. Dual-Doppler observations of these two organized systems are analyzed here, and the resulting latent heating profiles are compared with estimates from the V6 TMI algorithm. The primary advantage of the dual-Doppler estimates of latent heating is that they provide an "instantaneous" sample of the heating distribution at relatively high spatial resolution.

The main source of error in the calculation of the heating rate using (1) is the error in the derivation of the vertical velocity. Although the measurement of the horizontal winds and horizontal divergence from the dual-Doppler analysis is fairly accurate, vertical velocities are calculated from mass continuity by integrating the horizontal divergence vertically. In the current study, a variational scheme is utilized to adjust the divergence integral subject to the boundary conditions that the vertical velocity should be zero both at the surface and radar echo top; see O'Brien (1970). Nevertheless, errors in dual-Doppler estimates of vertical velocity are usually within 10%, but could be up to 30% in extreme cases, based upon an earlier study involving coincident sailplane observations (see Doviak and Zrnic 1993). Percentage errors of comparable magnitudes are expected in estimates of $Q_1$ using (1). As a result, error envelopes up to 30% are shown in the DDS estimates of $Q_1$ in the current study.

Rawinsonde analyses have been used previously by Olson et al. (1999), Yang and Smith (1999a, 2000), and Tao et al. (2001) to obtain latent heating time series for comparisons with satellite latent heating estimates. Because rawinsonde networks covering oceanic areas have relatively limited time and space sampling (two–four launches per day, and ~1 site per $10^4$ km$^2$), rawinsonde analyses are best suited for relatively large time-/space-scale comparisons.

In the present study, analyses of $Q_1$ from the Northern Enhanced Sounding Array (NESA) of the South China Sea Monsoon Experiment (SCSMEX) are compared with estimates of $Q_1 - Q_R$ from the V6 TMI algorithm. The rawinsonde sites associated with NESA, located in the northern portion of the South China Sea, are depicted in Fig. 2. The rawinsonde-based estimates of $Q_1$ are derived from the analyses of Johnson and Ciesielski (2002) for the period of 15 May–20 June 1998 over NESA. During the specified period, rawinsondes were launched from two to four times a day at stations along the perimeter of NESA and four times per day from Dongsha Island and the Research Vessel *Shiyan #3*, located near the center of the array. Outside of the

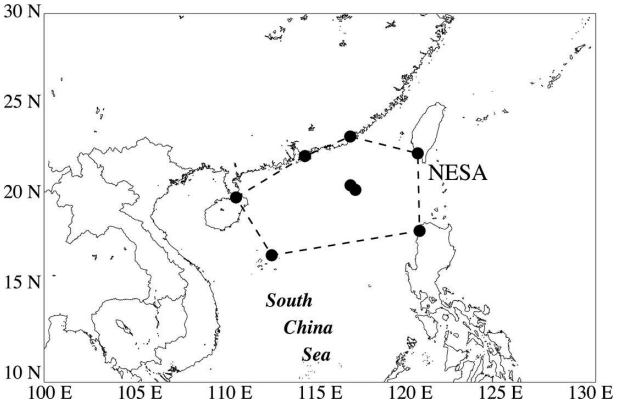


FIG. 2. Map of the northern South China Sea, showing the polygonal domain of NESA. Rawinsonde launch sites are located at the vertices of the polygon and on Dongsha Island and the Research Vessel *Shiyan #3* in the interior of the polygon. NESA was a domain of intensive observations during SCSMEX.

array, rawinsondes were typically launched from three to four times per day. The reader is referred to Johnson and Ciesielski (2002) for a description of procedures to analyze temperatures, specific humidities, and winds from the rawinsondes and model-based analyses to estimate mean $Q_1$ and $Q_2$ profiles within NESA at 0000, 0600, 1200, and 1800 UTC during the specified period. In addition to $Q_1$ and $Q_2$, these authors estimated the surface rain rate over NESA from the moisture budget,

$$\frac{c_p}{g}\int_{p_t}^{p_s} Q_2\, dp = L_v(P - E), \tag{2}$$

where the vertical integral of $Q_2$ is between the tropopause pressure $p_t$ and the surface pressure $p_s$; $L_v$ is the latent heat of vaporization, $P$ is the surface precipitation rate, and $E$ is the surface evaporation rate. Surface evaporation over NESA was obtained from reanalysis values, adjusted by shipboard flux measurements from the *Shiyan #3*; see Johnson and Ciesielski (2002) for a description of the procedure. Given the vertical integral of $Q_2$ and $E$, the surface precipitation rate was derived from (2).

Sampling errors in rawinsonde-based analyses for several sounding arrays were estimated by Mapes et al. (2003). They found that errors in NESA surface rainfall rates from the $Q_2$ budget are reduced to 1.3 mm day$^{-1}$, or about 30% of the long-term mean rain rate, using 3-day averages. Similar averaging reduces the error in the altitude of the peak $Q_1$ to 47 hPa, or about 800 m (at 7 km altitude), while a 30-day average will result in an error of 15 hPa or about 250 m (at 7 km altitude) in the altitude of the peak $Q_1$. Therefore, in order to reduce errors resulting from the relatively coarse temporal sampling of NESA by the TMI (about 1.4 day$^{-1}$) and rawinsondes, a 3-day running mean filter is applied to

the domain-averaged estimated heating profiles and surface rain rates within NESA from both the TMI and the rawinsonde analyses. Mean heating profiles and rain rates are also calculated for the entire 15 May–20 June 1998 period.

## 3. Surface rain-rate intercomparisons

### *a. Footprint resolution*

Prior to the evaluation of lower-resolution products, instantaneous maps of surface rain rate from V6 and V5 TMI, as well as collocated rain estimates from Kwajalein GV radar and PR, are compared to illustrate changes in the TMI algorithm.

The images in the left panels of Fig. 3 illustrate changes in the TMI algorithm estimates resulting from the revised, higher-resolution geographic database used in the algorithm to separate ocean, coast, and land regions in V6. The Kwajalein GV radar observations in the middle panel correspond to the TRMM overpass at 1700 UTC 24 August 1998. Although TMI observed the precipitation system near the Kwajalein GV site during this overpass, the system was outside the boundaries of the PR swath, and therefore only the GV rain map shown in the middle left-hand-side panel is compared with the V6 and V5 TMI estimates. Note that in the proximity of Kwajalein and the Namu Atoll to the southeast, the pattern of V5 rain-rate estimates differs from the radar pattern. This behavior of the V5 estimates is due to the classification in V5 of very small islands as "coast," even though the predominant surface type is ocean. Rain estimates are affected because only scattering signatures at 85 GHz from ice-phase precipitation are utilized in regions classified as coast. The indirect inference of rain from ice-scattering signatures leads to errors in the estimated precipitation patterns and intensities. In V6, the revised geographic database reclassifies small islands as "ocean" if the percentage of land in the nominal TMI footprint is minimal (see Part I, section 3e). Both rain emission and ice-scattering data are used in the TMI algorithm for footprints classified as ocean, and because Kwajalein and neighboring atolls are classified as ocean in V6, more realistic patterns of surface precipitation are obtained.

The right panels of Fig. 3 are based upon observations coinciding with the TRMM overpass at 1700 UTC 28 October 1998. In this case most of the precipitation fell beyond the range of the Kwajalein GV radar, and so PR rain estimates, shown in the middle panel, are compared with V6 (V5) TMI rain estimates in the top (bottom) panel. Because the PR has a relatively high spatial resolution and a better ability to detect light rain, the gradients of light rain along the edges of the rain system in the right-middle panel are considered accurate. (Note that the minimum detectable surface rain rate from PR is roughly 0.3 mm $h^{-1}$, corresponding to a minimum detectable signal of 18 dB$Z$.) The pattern of rainfall derived from V6 is generally more consistent with the PR estimate, while the V5 rain pattern exhibits none of the gradients along the precipitation boundaries seen in the PR imagery. The improved rain patterns of the V6 estimates are mainly attributed to the expanded cloud radiative model database supporting V6; the expanded database includes a better representation of isolated convection and weak precipitation events relative to the V5 supporting database (see Part I).

Because different ocean/coast/land classifications are used in the V5 and V6 TMI algorithms, in all of the plots and statistical analyses to follow only latitude–longitude grid boxes with essentially complete coverage (90% of the grid box area) by TMI, GV radar, and PR, with all footprints classified as ocean by the V5 TMI algorithm, are considered. The V5 classification is used because the focus of this study is changes in the ocean precipitation/latent heating estimation method, and the V5 ocean footprints are a subset of the V6 ocean footprints. Also, data pairs for which both sensors yield zero rain rates are excluded from the analyses in order to emphasize the skill of the algorithms in raining regions.

### *b. Instantaneous, 0.5° × 0.5° estimates*

Displayed in Fig. 4 are scatterplots of oceanic instantaneous 0.5° × 0.5° mean surface rain rates at the Kwajalein site from V6 and V5 TMI versus Kwajalein GV radar and PR estimates, drawn from the 21 selected rain events during 1998. Statistics of these intercomparisons are provided in Table 1. It may be noted from the plots in Fig. 4a that rain-rate estimates from both the V6 and V5 TMI show reasonable agreement with the GV radar and PR near Kwajalein, although differences between the rain estimates are still evident. The correlations between the TMI estimates and either GV or PR improve slightly in the progression from V5 to V6, and V6 estimates are less biased and have lower random error. Convective rain-rate estimates (Fig. 4b) are less correlated with GV or PR than total rain-rate estimates, because of the less direct inference of convective or stratiform rain type from the passive microwave data. It is expected that the GV radar or PR can provide a more detailed picture of precipitation structure than TMI, although fundamental differences in the definitions of convective and stratiform rain types from GV, PR, and TMI can also lead to differences in the estimated convective/stratiform rain proportion.

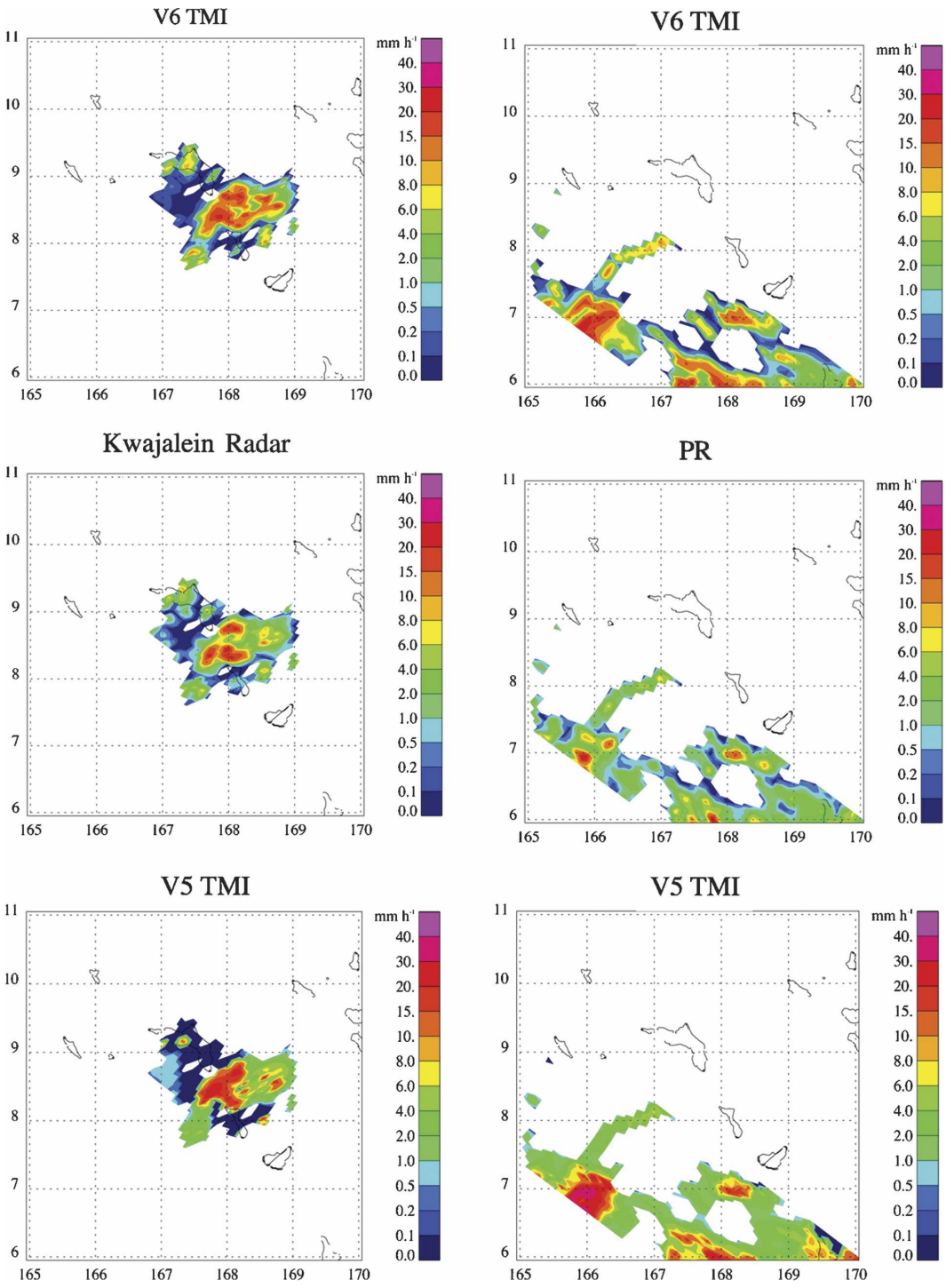


FIG. 3. Comparisons of instantaneous surface rain rates near the Kwajalein Atoll from matched GV radar, PR, and TMI at TMI product resolution (14 km × 14 km). (left) The surface rain-rate estimates from (top) V6 TMI, (middle) the Kwajalein radar, and (bottom) V5 TMI at approximately 1700 UTC 24 Aug 1998, and (right) the rain-rate estimates from V6 TMI, PR, and V5 TMI at approximately 1700 UTC 28 Oct 1998 are shown.

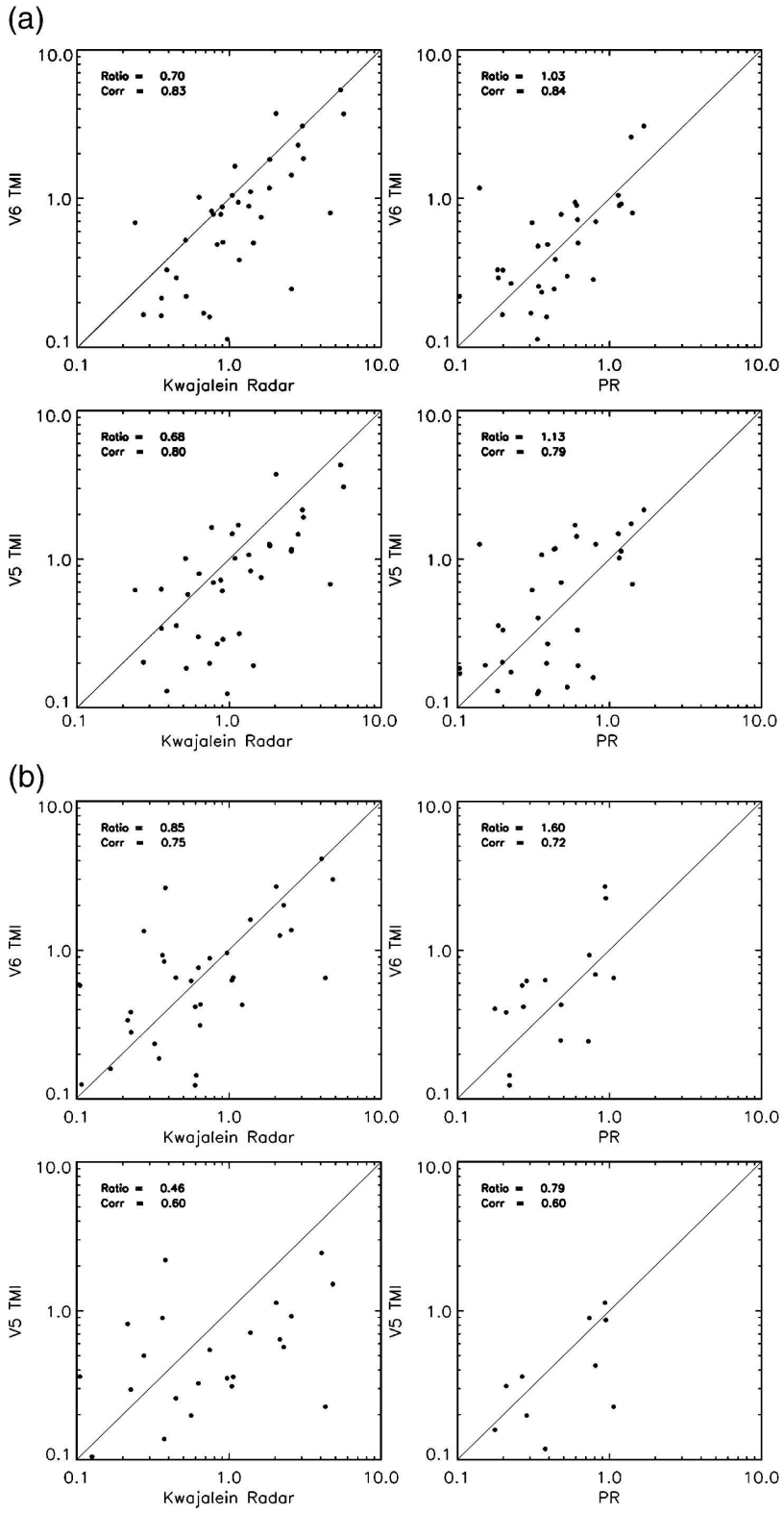


FIG. 4. Scatterplots of instantaneous, 0.5° × 0.5° average (a) total surface rain rates and (b) convective rain rates from [top of (a) and (b)] V6 TMI and [bottom of (a) and (b)] V5 TMI vs (left) Kwajalein radar and (right) PR, based upon 21 selected TRMM overpasses of Kwajalein in 1998.

TABLE 1. Comparison of instantaneous 0.5° × 0.5° precipitation products over ocean at the Kwajalein GV site during 1998. Respectively, V6 and V5 are the statistics of the TMI surface rain rate estimates from the version-6 and version-5 algorithms. CONV is the statistics of the V6 TMI estimates of convective rain rate.

| | TMI vs GV | | | TMI vs PR | | |
|---|---|---|---|---|---|---|
| Statistic | V6 | V5 | CONV | V6 | V5 | CONV |
| Sample | 62 | 62 | 54 | 72 | 72 | 54 |
| TMI mean | 0.67 | 0.65 | 0.60 | 0.29 | 0.32 | 0.29 |
| Ratio of means | 0.70 | 0.68 | 0.85 | 1.03 | 1.13 | 1.60 |
| Error std dev | 0.71 | 0.78 | 0.73 | 0.30 | 0.32 | 0.36 |
| Correlation | 0.83 | 0.80 | 0.75 | 0.84 | 0.79 | 0.72 |

Although the evaluation of TRMM products near the ground validation sites has the advantage of the availability of rain gauge–calibrated ground radar observations (Wolff et al. 2005), the errors statistics based upon GV radar represent only local conditions over the period of study. Because of the large spatial and temporal variations of precipitation, more general conclusions can be made from global comparative datasets. Therefore, all V6 and V5 instantaneous TMI precipitation estimates from July 2000 over ocean areas are compared with coincident PR estimates at 0.5° × 0.5° resolution. Presented in Fig. 5a are scatterplots of the collocated TMI and PR estimates; statistics of the comparisons are given in Table 2. Again, both the V6 and V5 estimates of surface rain rate are well correlated with PR estimates, with only a slight reduction in the correlation coefficient of the V6 estimates. However, the V6 estimates have less bias and lower random error in relation to the V5 estimates.

Estimates of the convective rain rate are less correlated with PR, and the bias and random error of these estimates is greater than the corresponding statistics of total rain. The less direct inference of convective precipitation structure from the TMI is the primary reason for the greater scatter of TMI convective rain rates relative to PR. Note that the V6 convective rain estimates are more high biased with respect to the PR than the V5 estimates. The greater mean departure of V6 convective rain estimates is mainly attributed to the revised definition and classification of convective/stratiform rain areas in the V6 algorithm (see Part I, sections 3d and 3g), whereas the classification used in V5 is calibrated against the PR classification (see Olson et al. 2001).

More insight into the estimation of convective and stratiform rain intensities by V6 is gained by considering a separation of the rain data based upon the PR classification of convective/stratiform rain areas. In Fig. 5b, the rain data are reclassified as "primarily convective," for which the PR convective rain proportion over each half-degree box is greater than 50% of the total PR rain, and "primarily stratiform," for which the PR convective proportion is less than 50%. Although this partitioning is only approximate, both V5 and V6 TMI estimates for each half-degree box are given the same classification, and therefore differences in estimated convective and stratiform rain *intensities* are isolated.

As seen in Fig. 5b, there is not an obvious difference between the scatterplots of the V6 and V5 primarily convective data, but a significant decrease in the average intensity of V6 stratiform rains relative to V5 is evident. The high bias of TMI rain estimates with respect to PR estimates decreases from 21% to 2% in stratiform areas. The change in stratiform rainfall intensity is due to the revision of the method for determining convective and stratiform rain proportions in the TMI algorithm. In V5, the area fraction of convective precipitation within the nominal sensor footprint was used to constrain the selection of simulated precipitation profiles in the algorithm's supporting database; see Kummerow et al. (2001). In addition, the proximity of a footprint to convection was also used as a constraint; therefore, even footprints with no convective coverage might be assigned a quasi-convective precipitation structure if they were adjacent to footprints classified as convective. This "blurring" of the convective/stratiform characterization led to overestimates of rain intensity in stratiform regions. In V6, in addition to the convective area constraint, a constraint on the total rain area is imposed; see Part I. As a result, a better indicator of the relative proportions of convective and stratiform rain flux is supplied to the algorithm. Also, the constraint on the proximity to convection is removed to produce a more distinct separation of convective and stratiform rain regions in a given mesoscale convective system. This more distinct separation leads to lower-intensity stratiform rains and a lower overall bias of stratiform and total rain from the V6 algorithm, as indicated in Fig. 5b. The discrepancy between the basic definitions of convective/stratiform rain areas in the V6 and PR algorithms will be the focus of a future study.

Overlaid on the V6 scatterplot of Fig. 5a is a fit to the mean algorithm-derived estimate of error standard deviation as a function of rain rate (see Part I),

$$\sigma_{\overline{P}} \cong 0.930 \ln(\overline{P} + 1 \text{ mm h}^{-1}). \quad (3)$$

Here, $\sigma_{\overline{P}}$ and $\overline{P}$ have units of millimeters per hour. The expression (3) represents only that portion of the

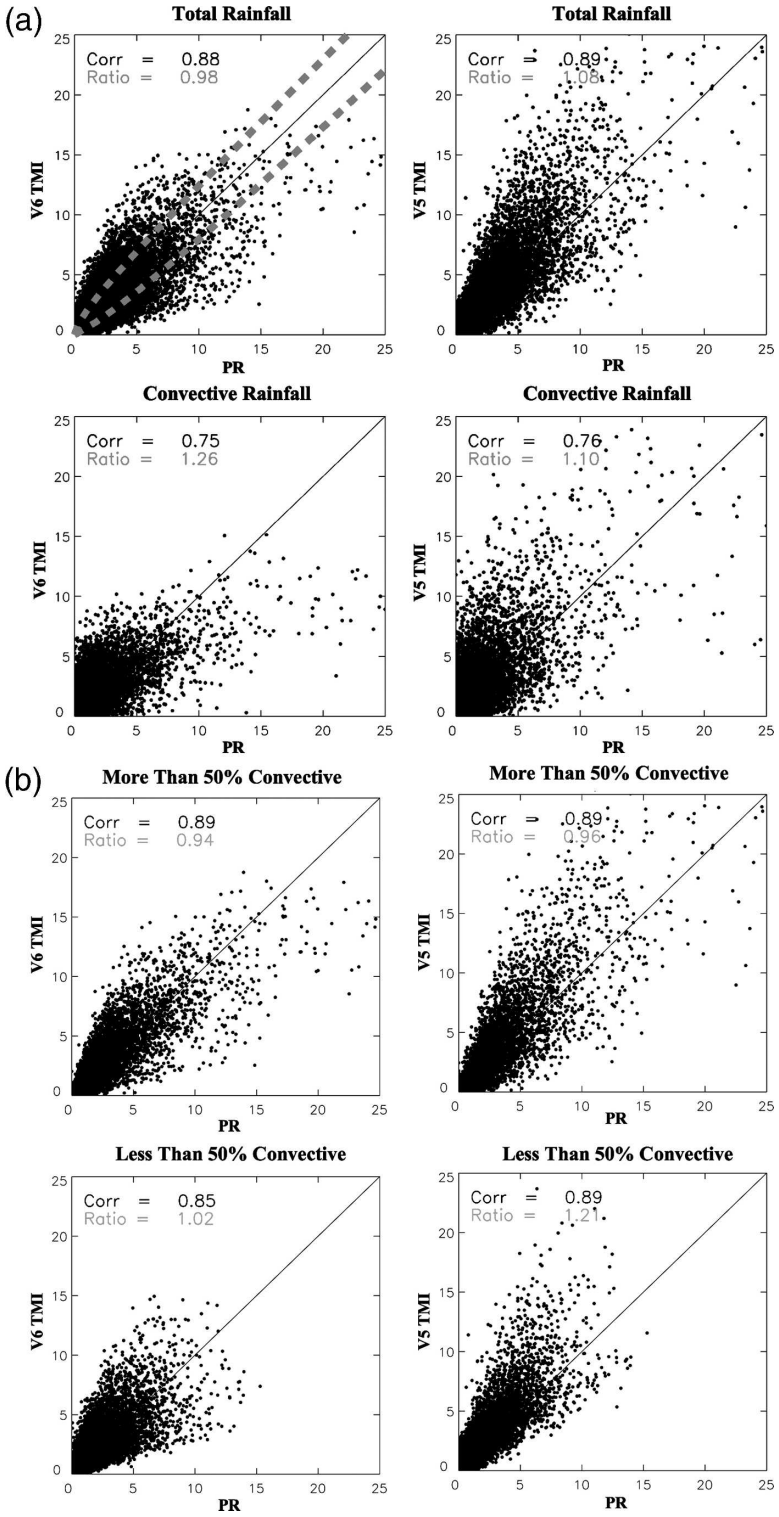


FIG. 5. (a) Scatterplots of instantaneous, 0.5° × 0.5° average total (top) surface rain rates and (bottom) convective rain rates from (left) V6 TMI and (right) V5 TMI, vs PR. (b) Scatterplots of instantaneous, 0.5° × 0.5° average total surface rain rates for which the PR convective fraction is (top) greater than 50% and (bottom) less than 50% from (left) V6 TMI and (right) V5 TMI, vs PR. Plots are based upon all collocated observations over ocean from July 2000. Overlaid on the V6 TMI plot of total surface rain rates in (a) are bounds of the estimated mean error (dashed lines; see text for description).

TABLE 2. Comparison of instantaneous 0.5° × 0.5° precipitation products over ocean during July 2000. Respectively, V6 and V5 are the statistics of the TMI surface rain rate estimates from the V6 and V5 algorithms. CONV is the statistics of the V6 TMI estimates of convective rain rate.

| TMI vs PR | | | |
|---|---|---|---|
| Statistic | V6 | V5 | CONV |
| Sample | 258 558 | 258 558 | 119 201 |
| TMI mean | 0.26 | 0.28 | 0.33 |
| Ratio of means | 0.98 | 1.08 | 1.26 |
| Error std dev | 0.44 | 0.50 | 0.58 |
| Correlation | 0.88 | 0.89 | 0.75 |

algorithm random error resulting from the limited information content of the radiometer data. It is apparent that the assumption of zero rain-rate error in footprints classified as nonraining is a deficiency of the model, because significant errors are seen near the origin of the scatterplot. The relative contributions of errors resulting from uncertainties in PR estimates, spatial sampling mismatches, and errors in cloud radiative modeling have yet to be determined, but the mean algorithm estimate of error given by (3), modified by errors in nonraining footprints, may be useful for data assimilation applications. A more specific estimate of the error in each half-degree rain estimate is given by the full model [Eq. (8) in Part I], but this requires an aggregation of the errors at footprint scale.

Variations of precipitation system structure and frequency of occurrence over the globe should lead to inhomogeneous distributions of error in rain-rate estimates from spaceborne sensors, because of the limited information these sensors provide with regard to the physical characteristics of observed precipitation systems. Berg et al. (2002) examined the systematic differences in satellite-based rain-rate estimates in the east Pacific (EP) and west Pacific (WP) and linked these to differences in precipitation structure. Here, V6 and V5 TMI rain-rate estimates over the tropical oceans from July 2000 are broken down by region to uncover possible variations in error statistics.

Presented in Fig. 6 are statistics of TMI and PR rain-rate comparisons at 0.5° resolution, derived from TRMM observations of five selected tropical 10° × 10° areas, including areas in the WP, EP, Atlantic Ocean (AO), Indian Ocean (IO), and SCS. The boundaries of these areas are given in Table 3. It may be noted from the figure that the typical high biases of the V5 TMI estimates are generally reduced in the V6 estimates, and random errors decrease. This result holds independent of the specified region, even though the correlations of the estimates with collocated PR rain rates are nearly unchanged. The implication of these regional tests is that the modifications of the TMI algorithm in the progression from V5 to V6 corrected basic deficiencies that previously affected algorithm performance throughout the Tropics; however, based upon the limited samples of regional data utilized here, no general conclusions can be made.

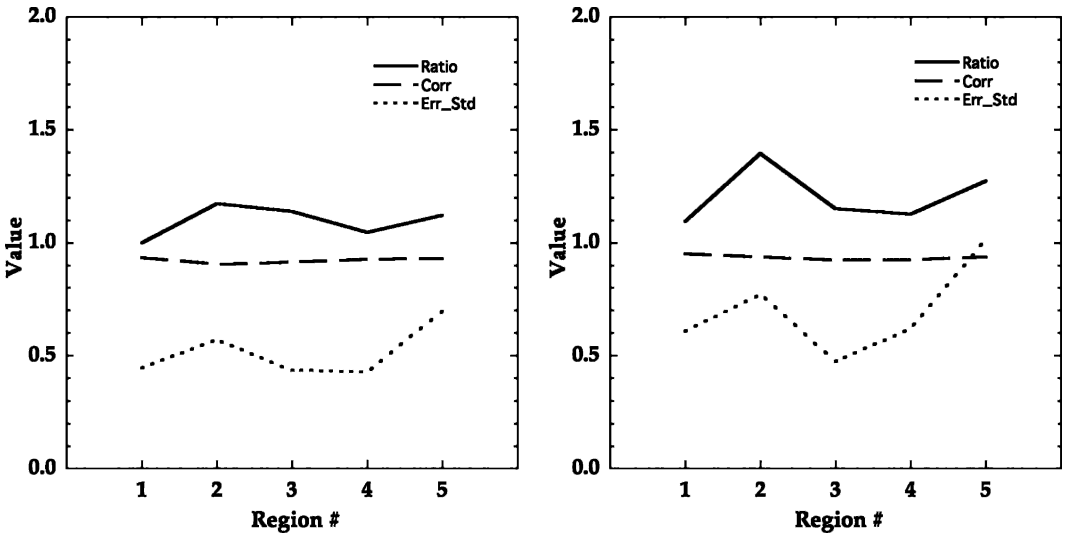


FIG. 6. Bivariate statistics for the intercomparison of instantaneous 0.5° × 0.5° average surface rain rates from (left) V6 TMI and (right) V5 TMI, vs PR for the five selected tropical oceanic domains defined in Table 3. Abscissa indices 1, 2, 3, 4, and 5 correspond to the western Pacific Ocean, eastern Pacific Ocean, Atlantic Ocean, Indian Ocean, and South China Sea, respectively. Plotted are the TMI/ PR bias ratio (solid line), correlation coefficient (dashed line), and error standard deviation (dotted line, mm $h^{-1}$).

TABLE 3. Boundaries of 10° × 10° domains selected for regional analyses presented in Fig. 6.

| Region | Latitude–longitude domain |
|---|---|
| West Pacific | 5°S–5°N, 150°–160°E |
| East Pacific | 0°–10°N, 105°–95°W |
| Atlantic Ocean | 0°–10°N, 40°–30°W |
| Indian Ocean | 5°S–5°N, 80°–90°E |
| South China Sea | 10°–20°N, 110°–120°E |

### c. *Monthly 2.5° × 2.5° estimates*

Intercomparisons of monthly mean 2.5°-resolution V6 and V5 TMI and PR rain-rate estimates over ocean from July 2000 are presented in Fig. 7. Note that these monthly means are derived only from space- and time-coincident TMI and PR observations; therefore, differences in the monthly means arise from TMI or PR algorithm errors rather than differences in sampling. It may be inferred from the figure that although the correlations of the monthly 2.5° V6 and V5 estimates to PR estimates are the same, V6 estimates exhibit less overall bias with respect to PR.

Typically, greater averaging of passive microwave rain estimates has the effect of reducing the algorithm random error relative to the variance of the rain data, resulting in higher correlations of rain estimates with respect to independent data. Here, indeed, the correlations of both V6 and V5 rain estimates with respect to the PR are greater than the correlations of the instantaneous 0.5° averages with respect to PR, shown previously (see Table 2). However, the question remains: what proportion of the scatter seen in Fig. 7 is due to purely random error, and what proportion is due to regional biases of the algorithm that may be either positive or negative depending on the location of a given 2.5° grid box, producing additional scatter?

The data are analyzed further in an attempt to determine what proportion of the scatter in Fig. 7 is due to purely random algorithm errors and what proportion is due to regionally varying systematic errors. The local bias of algorithm estimates is determined by taking the mean difference between collocated, instantaneous 0.5° TMI and PR estimates over the month in each 2.5° grid box,

$$b_{\langle\overline{P}\rangle\mathrm{alg}} = \frac{1}{N}\sum_{i=1}^{N}(\overline{P}_{\mathrm{TMI}i} - \overline{P}_{\mathrm{PR}i}), \tag{4}$$

where $N$ is the number of collocated 0.5° estimates contributing to the monthly average. The corresponding random error in monthly 2.5° rain rates is estimated from

$$\sigma_{\langle\overline{P}\rangle\mathrm{alg}} \cong \frac{1}{N}\left(\sum_{i=1}^{N}\sigma^2_{\overline{P}\mathrm{alg}i}\right)^{1/2}, \tag{5}$$

where

$$\sigma^2_{\overline{P}\mathrm{alg}} = \frac{1}{N}\sum_{i=1}^{N}(\overline{P}_{\mathrm{TMI}i} - \overline{P}_{\mathrm{PR}i} - b_{\langle\overline{P}\rangle\mathrm{alg}})^2. \tag{6}$$

Here, the descriptor "alg" is used to differentiate between algorithm error and the sampling error described in Part I [see (9) in Part I]. Note also that the algorithm

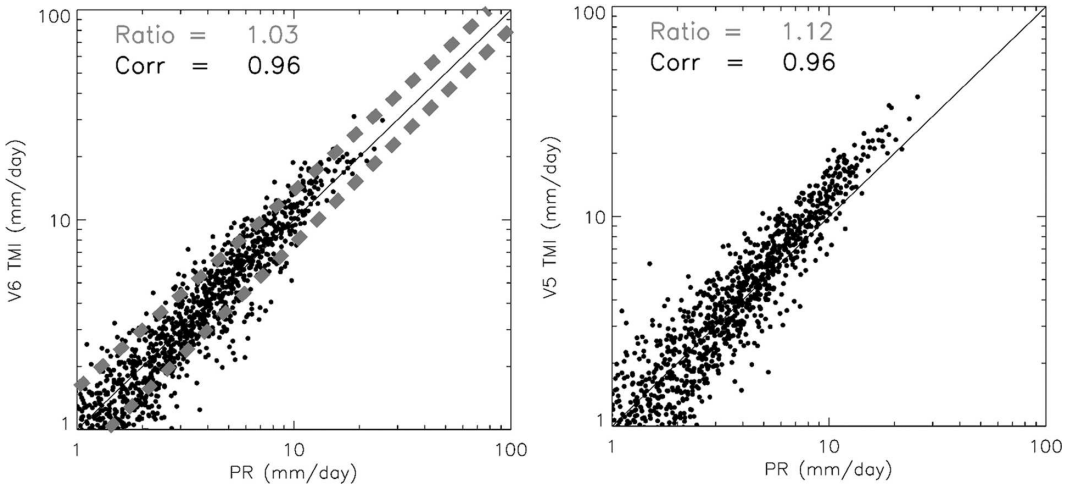


FIG. 7. Plots of monthly 2.5° × 2.5° resolution (left) V6 TMI and (right) V5 TMI rain-rate estimates, vs PR estimates, based upon collocated TMI and PR observations over ocean from July 2000. Superimposed on the V6 TMI rain rates are bounds of the estimated mean sampling error of TMI (heavy dashed lines, see text for description).

error derived from theoretical considerations in Part I [see (8) of Part I] was assumed to be random with zero mean, and this theoretical estimate is analogous to the observational estimate (6), above. The relation (4), on the other hand, gives an estimate of the algorithm systematic error in a monthly 2.5° estimate.

The July 2000 data over ocean are used to construct the histograms of $b_{\langle\overline{P}\rangle\text{alg}}/\sigma_{\langle\overline{P}\rangle\text{alg}}$ shown in Fig. 8. The solid curve is based upon the data and the estimate of the 0.5° error variance given by (6); the long-dashed curve employs instead the model given by (3) for the 0.5° error standard deviation as a function of $\overline{P}$ to calculate the error variance. The significance of these plots is that the ratio of bias-to-error standard deviation is a measure of the relative contributions of local systematic and random algorithm errors to monthly 2.5° estimates of rain rate—a narrow-peaked histogram implies a greater contribution from random errors, while a broad-peaked histogram indicates a greater contribution from systematic errors. Both estimates of the 0.5° error variances lead to histograms that are relatively broad in comparison with a theoretical Gaussian histogram with unit variance (also plotted in Fig. 8), for which systematic and random errors would make comparable contributions. This result suggests that in monthly 2.5° estimates of rain rate, the contribution of algorithm systematic errors tends to be greater than the algorithm random error contribution, which could explain the persistence of algorithm errors despite considerable averaging of estimates in time and space. Systematic algorithm errors could include errors in the supporting cloud radiative model simulations of the TMI supporting database or unrepresentative proportions of various precipitation system types in the database.

Two caveats pertaining to the foregoing analysis should be noted: First, although they are assumed to be smaller, random and systematic errors in the PR rain estimates could also contribute to the overall scatter seen in Fig. 7. Also, the random error calculation (5) does not account for error correlations of the 0.5° estimates, and these could lead to greater random errors and histograms that are more narrowly peaked than those in Fig. 8.

To provide some perspective on the relative magnitudes of rain algorithm error and sampling error, an estimate of the mean TMI temporal sampling error is overlaid on the V6 plot of Fig. 7. Following Bell and Kundu (2000), the percentage sampling error given by their (2.22) and (2.23) (see Part I) is represented as a function of the monthly mean rain rate at 2.5° resolution using a power-law fit, based upon the July 2000 data plotted in Fig. 9 of Part I,

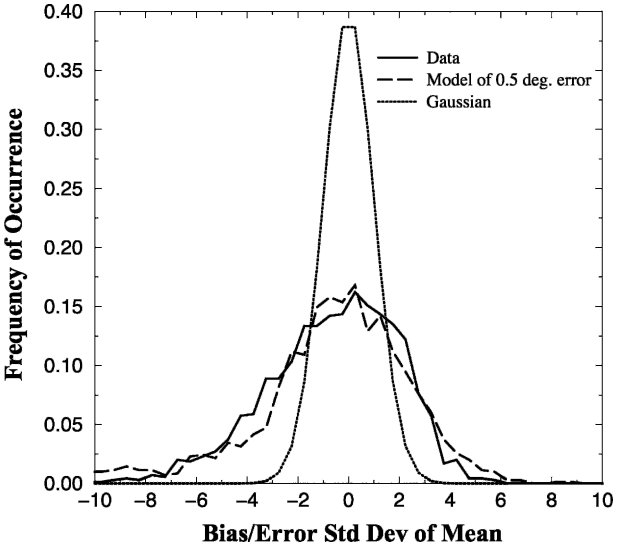


FIG. 8. Histograms of the ratios of estimated bias to error standard deviation, based upon TMI and PR observations over ocean from July 2000. Solid line is derived using the estimate of 0.5° error variance given by (6), and the dashed line incorporates the model of 0.5° error standard deviation given by (3). For comparison, a Gaussian distribution with unit variance is superimposed.

$$\frac{\sigma_{\langle\overline{P}\rangle}}{\langle\overline{P}\rangle} \times 100\% \cong 20.5\langle\overline{P}\rangle^{-0.130}. \tag{7}$$

From our Fig. 7 it may be noted that qualitatively, the mean TMI sampling error is comparable to the combined TMI and PR algorithm error. This result appears to contradict the assumption in previous studies that algorithm errors make a small contribution to the error in monthly means relative to sampling errors (Wilheit 1988; Bell et al. 1990; Bell and Kundu 2000). The assumption of relatively small algorithm errors would be correct if these errors were purely random with zero mean. The contribution of regionally varying systematic algorithm errors to the total algorithm error is relatively large, as indicated by Fig. 8, and therefore near parity of algorithm and sampling errors results at the monthly 2.5° scale.

## 4. Latent heating comparison results

### *a. Comparisons with dual-Doppler study estimates*

As noted in section 2, heating estimated from the DDS method is only an approximation to the total diabatic heating; however, in convectively active regions the vertical structure of the heating from the DDS analysis should be similar to that of $Q_1 - Q_R$. Figure 9 illustrates comparisons of the vertical heating profiles

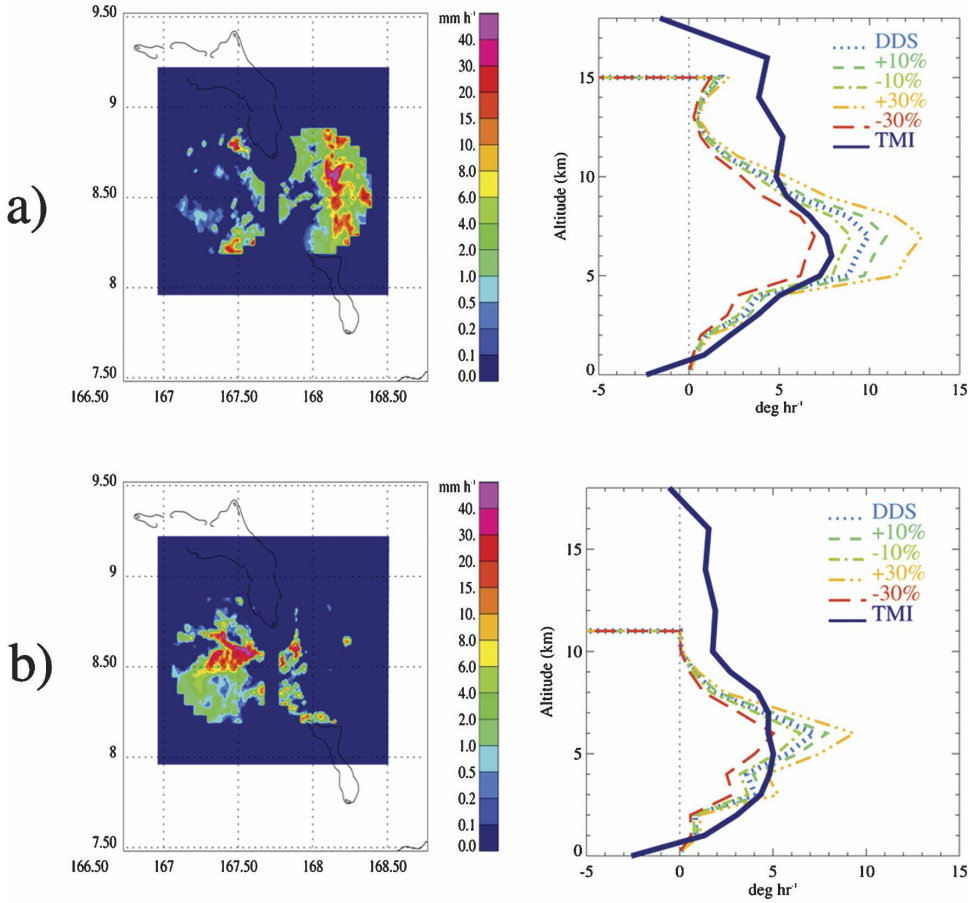


FIG. 9. Comparisons of V6 TMI and DDS heating profiles for two selected TRMM overpasses of the Kwajalein Atoll. (left) Plan views of surface rain rates from the Doppler radar measurements. (right) Vertical profiles of $Q_1 - Q_R$ from V6 TMI (solid line), overlaid on plots of estimated $Q_1$ from DDS (various dashed lines) for different assumed bias errors, ranging from 0% to 30%. Data (a) correspond to the TRMM overpass at approximately 1000 UTC 15 Aug 1999 and (b) correspond to the overpass at 1900 UTC 29 Jul 1999.

from V6 TMI and DDS for two selected cases from the Kwajalein site. Shown in Fig. 9a are fields coinciding with the TMI overpass at approximately 1000 UTC 15 August 1999, while the fields shown in Fig. 9b correspond to the overpass at 1900 UTC 29 July 1999.

The precipitation shown in the dual-Doppler radar lobes in Fig. 9a was produced by an organized mesoscale convective system that began as a westward-propagating convective line. The retrieved mean heating profile from TMI shows deep positive heating from 1 to 17 km, with a maximum near 6 km. Evaporative cooling is seen near the surface. Heating estimates from the DDS are limited in altitude by the height of the radar-detectable echo, and the vertical integral of radar-derived wind divergence is adjusted in the DDS to yield zero vertical velocity at echo top. Therefore, it usually follows that the more intense and extensive the rain system is, the deeper the DDS heating analysis. In this case, the mean DDS heating is limited to altitudes below 15 km. The DDS mean heating profile exhibits positive heating from the surface to 15 km, with a maximum near 7 km. The maximum DDS heating magnitude is greater than that derived from the TMI. Although the vertical distributions of heating from TMI and DDS are consistent from the surface to the level of maximum heating, the TMI heating in the upper troposphere generally exceeds the DDS heating.

The disturbance that produced the rain pattern shown in Fig. 9b was imbedded in an extensive east–west-oriented band of precipitation that approached Kwajalein from the south. The overall depth of the precipitation from this system was less than that of the preceding case, resulting in a shallower, less intense heating maximum derived from TMI. Similar to TMI, significant heating from the DDS is confined to altitudes less than 10 km, although the peak DDS heating

is greater than that of the TMI heating profile. The DDS heating maximum is sharper than the TMI maximum, but both analyses reveal maximum heating centered at 5–6-km altitude. As in the preceding case, the TMI algorithm yields weak heating in the upper troposphere that is not reflected in the DDS analysis.

There could be several reasons for the discrepancies between the mean TMI and DDS heating profiles. First, in applications to relatively intense precipitation systems, the TMI algorithm tends to bias heating estimates toward the mean of heating profiles stored in the algorithm's supporting database, and this could explain the broad, but relatively weak, heating profiles produced by the algorithm (see Part I, section 4). On the other hand, there is relatively large uncertainty in estimating the vertical velocity from the DDS method, and the condition of zero vertical velocity at echo top is a strong constraint on the analyzed heating. It may be noted from Fig. 9 that the magnitudes of heating profiles from TMI are generally located within the 30% error envelopes of the DDS heating profiles. High biases of the TMI profiles outside the DDS error envelopes occur in the upper troposphere, however.

Despite the noted discrepancies, these comparisons at the Kwajalein site illustrate the V6 TMI algorithm's potential, at least in the lower and midtroposphere, for capturing variations of latent heating vertical structure.

### b. Comparisons with rawinsonde-based estimates

Although comparisons of instantaneous latent heating estimates from TMI and DDS analyses are optimal from a sampling perspective, the limited number of collocated observations makes it impossible to draw any general conclusions. The SCSMEX NESA rawinsonde analyses described in section 2 are based upon limited temporal sampling (up to four per day), but they provide a continuous record of the evolution of diabatic heating over the SCSMEX intensive observing period. Here, 3-day running-mean estimates of rawinsonde $Q_1$ and surface rain rate (from the $Q_2$ budget; see section 2) are compared with similarly averaged TMI estimates (~1.4 per day sampling) for the period beginning with the monsoon onset in the South China Sea on 15 May, and extending to 20 June 1998.

The surface rain-rate time series from TMI and the rawinsonde analyses are shown in the top panel of Fig. 10. This comparison is a good indicator of the relative sampling of precipitation systems by the two methods over the prescribed period. Note that despite the rather limited temporal sampling by TMI and the rawinsondes, the 3-day mean surface rainfall rates are in fairly good agreement. The agreement between the

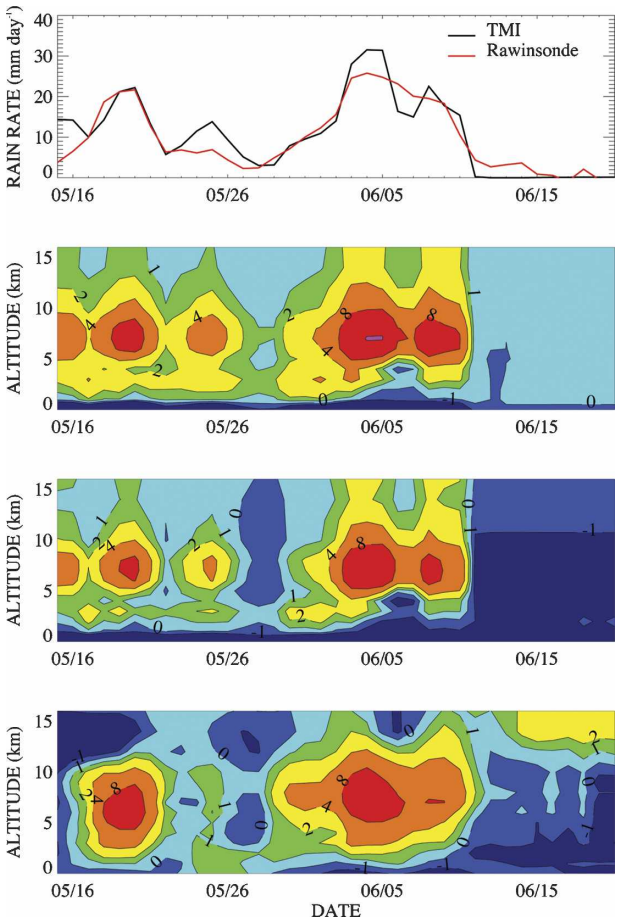


FIG. 10. Time series of (top to bottom) NESA-averaged surface rain rate, V6 TMI $Q_1 - Q_R$, V6 TMI $Q_1$, and rawinsonde analysis of $Q_1$ over the period of 15 May–20 June 1998, during SCSMEX. Surface rain rates are derived from both V6 TMI and the rawinsonde $Q_2$ budget. A 3-day running-mean filter is applied to all data in the time series. Heating profile time series are contoured at −1, 0, 1, 2, 4, and 8 K day$^{-1}$.

TMI and rawinsonde analyses may be attributed, in part, to the large-scale forcing of precipitation during the observing period. For example, Johnson et al. (2005) noted that in the 11-day period following monsoon onset (15–25 May), precipitation occurred nearly continuously within the range of the Bureau of Meteorology Research Center C-band polarimetric (C-POL) radar located at Dongsha Island. Precipitation that is more strongly correlated in time tends to reduce the effects of intermittent sampling. Nevertheless, there are periods during which TMI rain rates are biased relative to the rawinsonde estimates. For example, TMI estimates are high biased in the 3–4-day periods centered on 15 and 24 May and 4 June, and are low biased on 6–7 June.

A time series of $Q_1 - Q_R$ from TMI is shown in the

second panel of Fig. 10. To make a more consistent comparison with the rawinsonde heating estimates, however, a rough correction for radiative heating/cooling is added to the TMI $Q_1 - Q_R$ estimates to create the time series of TMI $Q_1$, shown in the third panel of Fig. 10. To make the correction, the net radiative heating/cooling profiles of Dopplick (1979) at 20°N latitude (March–May and June–August average; from his Figs. 6 and 7) are used to represent the mean radiative heating/cooling rate in NESA. The TMI $Q_1$ estimate may be more directly compared with $Q_1$ from the SCSMEX NESA rawinsonde analyses shown in the bottom panel of Fig. 10.

First, note that the primary differences between the TMI and rawinsonde $Q_1$ are correlated with differences in the estimates of surface rain rate. For example, the high bias of TMI $Q_1$ on 15 and 24 May, and the low bias of $Q_1$ on 7 June, are associated with similar biases in TMI surface rain rates at these times. Given that vertically integrated latent heating is approximately equal to $L_vP$, it is not surprising that biases in heating and surface rain rate are correlated. These biases may be attributed to the low temporal resolution of the TMI estimates; on average the frequency of the TMI observation of NESA was only ~1.4 day$^{-1}$, while the sounding frequency was ~2–4 day$^{-1}$.

Despite differences in temporal sampling by the TMI and rawinsondes, the correspondence of the TMI and rawinsonde $Q_1$ time series is reasonable. Heating maxima occur at about the same times and with similar magnitudes. Also, the transition from low-level heating starting on 28 May to a single midlevel maximum on 4 June is captured by the TMI and rawinsondes. One notable difference in the time series occurs after 11 June, when upper-level heating (altitudes greater than 12 km) is seen in the rawinsonde time series but not in the TMI series. Neither time series indicates significant precipitation during this period; and although the rawinsonde analysis suggests radiative heating of cirrus cloud, uncertainties in rawinsonde analyses are also greatest at high altitudes. Proper interpretation of the upper-tropospheric heating during this period will require greater scrutiny.

The mean TMI $Q_1 - Q_R$, $Q_1$, and rawinsonde $Q_1$ profiles for the 15 May–20 June 1998 period are presented in Fig. 11. After correcting for the effects of radiative heating, the TMI heating profile shows reasonable consistency with the rawinsonde profile. The main discrepancies are the excessive cooling in the TMI heating profile at the surface and below the melting level (~5 km). The cooling anomalies in the TMI profile could be explained by biases in the cloud-resolving model database; recent tests by S. Braun (2005, personal communication) indicate high biases in the precipitation water contents produced by cloud-resolving model simulations using standard bulk microphysics schemes. These biases would lead to a tendency for the V6 algorithm to select stratiform precipitation and heating vertical profiles over convective profiles from the algorithm's supporting database. A "stratiform bias" in estimated heating profiles would lead to stronger evaporative cooling at low levels and a deficiency of heating in the lower to midtroposphere. Investigations are underway to identify the causes of high biases in precipitation water contents produced by current cloud-resolving model simulations.

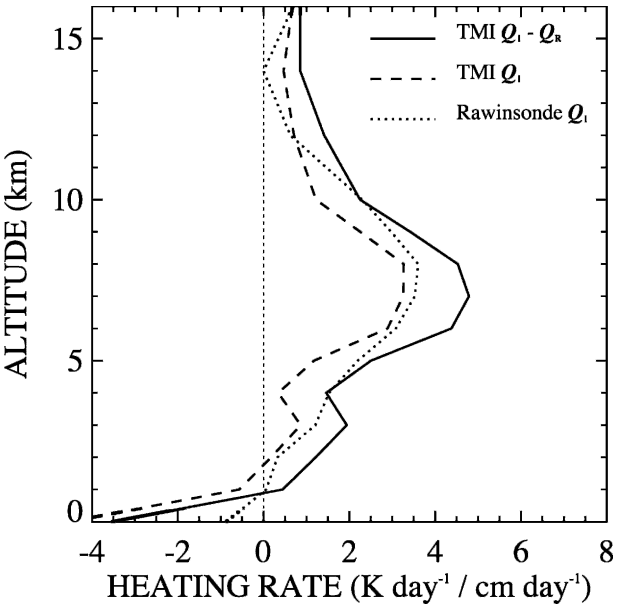


FIG. 11. Mean V6 TMI $Q_1 - Q_R$ (solid line), V6 TMI $Q_1$ (dashed line), and rawinsonde analysis $Q_1$ (dotted line) profiles for the period of 15 May–20 Jun 1998, over SCSMEX NESA.

## 5. Summary and discussion

The objective of this study is to provide an initial evaluation of rain-rate and latent heating estimates based upon an improved passive microwave radiometer algorithm (version 6), applied to TRMM Microwave Imager (TMI) radiance observations over ocean backgrounds. The formulation of the algorithm and improvements, along with estimates of random errors, are described in Part I of the study. The V6 TMI estimates are compared with independent, collocated estimates from rain gauge–calibrated radar at the Kwajalein Atoll ground validation site, as well as estimates from coincident spaceborne radar and an earlier radiometer algorithm applied to TMI data (version 5). Latent heat-

ing profiles from V6 TMI are compared with estimates based upon dual-Doppler observations at Kwajalein that are combined with thermodynamic profiles to obtain profiles of the vertical advection of dry static energy, a proxy for total diabatic heating. In addition, V6 TMI surface rain rate and latent heating time series are compared with time series derived from rawinsonde analyses of heat and moisture budgets over the Northern Enhanced Sounding Array of the South China Sea Monsoon Experiment.

In general, V6 TMI estimates of surface rain rate are consistent with estimates from ground-based or spaceborne radar, both in terms of instantaneous structure and quantitative precipitation amounts. The correlation of instantaneous 0.5°-resolution V6 TMI estimates with respect to radar-based estimates does not change appreciably relative to V5; however, the high bias previously noted in V5 estimates is significantly reduced. The overall reduced bias is attributed to the expanded cloud-resolving model database supporting the V6 algorithm, as well as the more consistent and specific convective/stratiform rain separation procedure, which together reduce the previous high bias in estimated stratiform rains. The global reduction of bias in V6 TMI (relative to V5) estimates appears to hold regionally as well, but to varying degrees. High biases in monthly 2.5°-resolution V6 TMI surface rain-rate estimates are also reduced relative to V5. The reduction of biases in satellite rain estimates is critical for current data assimilation and climate analysis applications.

The convective contribution to rain rate is generally more difficult to estimate than total rain rate, owing to ambiguities in the separation of convective and stratiform rains based upon radiance spatial structures and polarization signatures in the TMI data. Even the evaluation of TMI algorithm estimates of convective rain rate is difficult, given differences in the way convective and stratiform rain are defined in the algorithm relative to ground-based or spaceborne radar observations. The apparent reduction of the stratiform high bias in the V6 TMI estimates, previously noted, suggests that the current convective/stratiform rain separation is superior to the separation method applied in V5. Independent confirmation of this result will require an agreement on the definitions of convective and stratiform rain in TMI estimates and independent observations.

Although only limited comparisons of V6 TMI latent heating estimates with independent estimates are made in this study, the agreement between these estimates is reasonable, given the modest information content of the TMI data, differences in sampling between TMI and the independent measurement systems, and the general uncertainty in the independent estimates of heating. Comparisons of V6 TMI heating profiles with dual-Doppler profiles indicate that the altitude of maximum heating is tracked by the TMI estimates, although the detailed structure of the dual-Doppler profiles is not reproduced. The magnitude and altitude of the heating maximum in the mean SCSMEX NESA rawinsonde-derived profile is also reproduced in the TMI-estimated profile. There are notable biases in the V6 TMI heating estimates, however, including excessive cooling near the surface and just below the freezing level. These biases are likely the result of biases in the precipitation water contents of cloud-resolving model simulations that support the V6 TMI algorithm.

The potential for improvement of the V6 passive microwave radiometer algorithm depends mainly on what can be done to reduce biases in the precipitation/latent heating estimates. Bringing additional information into the estimation problem is one approach for reducing biases, but much of the radiative intensity and spatial gradient information in microwave imagery has already been exploited. Classification of storm type using the microwave observations and characterization of the storm environment from independent observations or model-based analyses could lead to more specific precipitation/latent heating estimates and reduced biases. Latent heating estimation should benefit most from storm-type/environment information, because the heating distribution is strongly linked to storm kinematics.

Because V6 estimates are sensitive to the type and distribution of cloud-resolving-model-simulated profiles in the algorithm's supporting database, there is great potential for reducing algorithm biases by creating supporting databases that are more consistent with naturally occurring profiles at the time/location where the algorithm is applied; see Shin and Kummerow (2003). A database constructed from hydrometeor profiles retrieved by applying a combined radar–radiometer algorithm to PR–TMI data has also been developed by the authors; see Grecu and Olson (2006). This type of database has the advantage that each hydrometeor profile is unbiased with respect to both PR and TMI observations and is independent of cloud-resolving model assumptions (although some limited assumptions concerning vertical particle-size distributions are made). In addition, the natural distribution of profiles appropriate for a specific radiometer algorithm application can be derived by repeated application of the combined PR–TMI algorithm and sorting of the resulting profiles by storm type, storm environment, or other contextual conditions. Cloud model simulations would still be required to associate an appropriate ver-

tical latent heating profile to each PR–TMI hydrometeor profile estimate.

The characterization of random errors in 0.5° × 0.5° V6 TMI estimates using the error model developed in Part I appears to be consistent with the magnitudes of errors determined from comparisons of TMI and PR rain-rate estimates. This model should be modified to account for errors in regions where the TMI algorithm identifies no rain, however. Another source of uncertainty is the potential error in simulated cloud-resolving model profiles that support the algorithm. If the algorithm's database is constructed from profiles derived from PR–TMI combined estimates, as previously discussed, then this error should be minimized. However, there will still be some uncertainty that a given profile in the database occurs with a prescribed frequency, and this uncertainty can only be resolved by long-term statistical evaluation of how that profile frequency fluctuates for specified contextual conditions.

Sampling error appears to explain only a portion of the total error in monthly 2.5°-resolution TMI estimates; algorithm errors make an equally important contribution, and these errors contain both random and systematic components. A preliminary analysis suggests that the contribution from systematic algorithm errors is often greater in magnitude than that of random algorithm errors at this time–space resolution. Systematic algorithm errors arise from the physical inconsistency or nonrepresentativeness of cloud-resolving-model-simulated profiles that support the algorithm.

Overall, the evaluation of TMI surface rainfall rate and latent heating based upon independent measurements, along with the results from Part I of this study, demonstrate that significant improvements have been made in V6 surface rain-rate estimates relative to those from V5, and that rain-rate and latent heating estimates from V6 have value for data assimilation and large-scale analysis applications.

*Acknowledgments.* TRMM datasets utilized in this study were accessed from the TRMM Science Data and Information System and the Goddard Space Flight Center Distributed Active Archive Center. David Wolff and David Marks of GSFC's Mesoscale Atmospheric Processes Branch provided analysis and helpful advice concerning Kwajalein ground validation radar estimates of rain rate. The University of Washington Mesoscale Group kindly supplied dual-Doppler radar datasets for selected cases. Estimates of $Q_1$ and surface rain rate based upon the SCSMEX rawinsonde network were provided by Paul Ciesielski and Richard Johnson of Colorado State University, whose expert advice is gratefully acknowledged. This research was supported by the NASA TRMM, Global Water and Energy Cycle, and Global Precipitation Measurement projects.

## REFERENCES

Awaka, J., T. Iguchi, and K. Okamoto, 1998: Early results on rain type classification by the Tropical Rainfall Measuring Mission (TRMM) precipitation radar. *Proc. Eighth URSI Commission F Triennial Open Symp.*, Aveiro, Portugal, International Union of Radio Science, 143–146.

Bell, T. L., and P. K. Kundu, 2000: Dependence of satellite sampling error on monthly averaged rain rates: Comparison of simple models and recent studies. *J. Climate,* **13,** 449–462.

——, A. Abdullah, R. L. Martin, and G. R. North, 1990: Sampling errors for satellite-derived tropical rainfall: Monte Carlo study using a space-time stochastic model. *J. Geophys. Res.,* **95,** 2195–2205.

Berg, W., C. Kummerow, and C. Morales, 2002: Differences between East and West Pacific rainfall systems. *J. Climate,* **15,** 3659–3672.

Cifelli, R., and S. A. Rutledge, 1998: Vertical motion, diabatic heating, and rainfall characteristics in North Australia convective systems. *Quart. J. Roy. Meteor. Soc.,* **124,** 1133–1162.

Davies-Jones, R. P., 1979: Dual-Doppler radar coverage area as a function of measurement accuracy and spatial resolution. *J. Appl. Meteor.,* **18,** 1229–1233.

Dopplick, T. G., 1979: Radiative heating of the global atmosphere. *J. Atmos. Sci.,* **36,** 1812–1817.

Doviak, R. J., and D. S. Zrnic, 1993: *Doppler Radar and Weather Observations*. 2d ed. Academic Press, 562 pp.

——, P. S. Ray, R. G. Strauch, and L. J. Miller, 1976: Error estimation in wind fields derived from dual-Doppler radar measurement. *J. Appl. Meteor.,* **15,** 868–878.

Grecu, M., and W. S. Olson, 2006: Bayesian estimation of precipitation from satellite passive microwave observations using combined radar–radiometer retrievals. *J. Appl. Meteor. Climatol.*, **45,** 416–433.

Hou, A. Y., S. Q. Zhang, and O. Reale, 2004: Variational continuous assimilation of TMI and SSM/I rain rates: Impact on GEOS-3 hurricane analyses and forecasts. *Mon. Wea. Rev.,* **132,** 2094–2109.

Iguchi, T., T. Kozu, R. Meneghini, J. Awaka, and K. Okamoto, 2000: Rain-profiling algorithm for the TRMM precipitation radar. *J. Appl. Meteor.,* **39,** 2038–2052.

Johnson, R. H., and G. S. Young, 1983: Heat and moisture budgets of tropical mesoscale anvil clouds. *J. Atmos. Sci.,* **40,** 2138–2147.

——, and P. E. Ciesielski, 2002: Characteristics of the 1998 summer monsoon onset over the northern South China Sea. *J. Meteor. Soc. Japan,* **80,** 561–578.

——, S. L. Alves, P. E. Ciesielski, and T. D. Keenan, 2005: Organization of oceanic convection during the onset of the 1998 east Asian summer monsoon. *Mon. Wea. Rev.,* **133,** 131–138.

Krishnamurti, T. N., and Coauthors, 2001: Real-time multianalysis–multimodel superensemble forecasts of precipitation using TRMM and SSM/I products. *Mon. Wea. Rev.,* **129,** 2861–2883.

Kummerow, C., and Coauthors, 2001: The evolution of the Goddard profile algorithm (GPROF) for rainfall estimation from passive microwave sensors. *J. Appl. Meteor.,* **40,** 1801–1820.

Liao, L., R. Meneghini, and T. Iguchi, 2001: Comparisons of rain

rate and reflectivity factor derived from the TRMM precipitation radar and the WSR-88D over the Melbourne, Florida, site. *J. Atmos. Oceanic Technol.,* **18,** 1959–1974.

Mapes, B. E., P. E. Ciesielski, and R. H. Johnson, 2003: Sampling errors in rawinsonde-array budgets. *J. Atmos. Sci.,* **60,** 2697–2714.

O'Brien, J. J., 1970: Alternative solutions to the classical vertical velocity problem. *J. Appl. Meteor.,* **9,** 197–203.

Olson, W. S., C. D. Kummerow, Y. Hong, and W.-K. Tao, 1999: Atmospheric latent heating distributions in the Tropics derived from passive microwave radiometer measurements. *J. Appl. Meteor.,* **38,** 633–664.

——, Y. Hong, C. D. Kummerow, and J. Turk, 2001: A texture-polarization method for estimating convective/stratiform precipitation area coverage from passive microwave radiometer data. *J. Appl. Meteor.,* **40,** 1577–1591.

——, and Coauthors, 2006: Precipitation and latent heating distributions from satellite passive microwave radiometry. Part I: Improved method and uncertainties. *J. Appl. Meteor. Climatol.,* **45,** 702–720.

Petty, G. W., 1995: Frequencies and characteristics of global oceanic precipitation from shipboard present-weather reports. *Bull. Amer. Meteor. Soc.,* **76,** 1593–1616.

Schumacher, C., and R. A. Houze Jr., 2000: Comparison of radar data from the TRMM satellite and Kwajalein oceanic validation site. *J. Appl. Meteor.,* **39,** 2151–2164.

Shin, D.-B., and C. Kummerow, 2003: Parametric rainfall retrieval algorithms for passive microwave radiometers. *J. Appl. Meteor.,* **42,** 1480–1496.

Tao, W.-K., and Coauthors, 2001: Retrieved vertical profiles of latent heat release using TRMM rainfall products for February 1998. *J. Appl. Meteor.,* **40,** 957–982.

Wilheit, T. T., 1988: Error analysis for the Tropical Rainfall Measuring Mission (TRMM). *Tropical Rainfall Measurements*, J. S. Theon and N. Fugono, Eds., A. Deepak, 377–385.

Wolff, D. B., D. A. Marks, E. Amitai, D. S. Silberstein, B. L. Fisher, A. Tokay, J. Wang, and J. L. Pippitt, 2005: Ground validation for the Tropical Rainfall Measuring Mission (TRMM). *J. Atmos. Oceanic Technol.,* **22,** 365–380.

Yanai, M., S. Esbensen, and J.-H. Chu, 1973: Determination of bulk properties of tropical cloud clusters from large-scale heat and moisture budgets. *J. Atmos. Sci.,* **30,** 611–627.

Yang, S., and E. A. Smith, 1999a: Moisture budget analysis of TOGA COARE area using SSM/I-retrieved latent heating and large-scale $Q_2$ estimates. *J. Atmos. Oceanic Technol.,* **16,** 633–655.

——, and ——, 1999b: Four-dimensional structure of monthly latent heating derived from SSM/I satellite measurements. *J. Climate,* **12,** 1016–1037.

——, and ——, 2000: Vertical structure and transient behavior of convective–stratiform heating in TOGA COARE from combined satellite–sounding analysis. *J. Appl. Meteor.,* **39,** 1491–1513.